Cell Reports
Physical Science

The case of the vanishing perovskite layer

Graphical abstract

Highlights

- Charge transport layer deposition damages layered perovskite passivation
- The layers are dissolved by polar solvent additives or damaged by small molecules
- Optimal device performance correlates with no crystalline layered perovskite
- Isolated bilayers are poor representations of what is actually present in a device

Authors

Marcin Giza, Fraser J. Angus,
Wai Kin Yiu, ..., Graeme Cooke,
Elisabetta Arca, Pablo Docampo

Correspondence

pablo.docampo@bcmaterials.net

In brief

Giza et al. identify that charge transport layer deposition greatly disrupts thin layers of layered perovskite commonly utilized in perovskite solar cells. The optimized deposition approaches for N-I-P and P-I-N devices are found to have independently converged on a final architecture that contains negligible quantities of crystalline layered perovskite passivation.

Giza et al., 2025, Cell Reports Physical Science *6*, 102890
October 15, 2025 © 2025 The Authors. Published by Elsevier Inc.
https://doi.org/10.1016/j.xcrp.2025.102890

CellPress

Cell Reports
Physical Science

CellPress
OPEN ACCESS

Article

The case of the vanishing perovskite layer

Marcin Giza,[1] Fraser J. Angus,[1] Wai Kin Yiu,[1,2] Madeleine McRoberts,[1] Benjamin Vella,[3] Jingbo Wang,[2] Aleksandra B. Djurišić,[2,4] Graeme Cooke,[1] Elisabetta Arca,[5] and Pablo Docampo[1,6,7,*]
[1]University of Glasgow, School of Chemistry, G12 8QQ Glasgow, UK
[2]University of Hong Kong, Department of Physics, Pokfulam Road, Hong Kong, China
[3]University of Strathclyde, Institute of Pharmacy and Biomedical Sciences, G4 0RE Glasgow, UK
[4]Institute Ruđer Bošković, Bijenička 54, 10000 Zagreb, Croatia
[5]Newcastle University, School of Mathematics, Statistics and Physics, NE1 7RU Newcastle upon Tyne, UK
[6]BCMaterials, Edif. Martina Casiano, Place 3 Parque Cientifico, 48940 Leioa, Spain
[7]Lead contact
*Correspondence: pablo.docampo@bcmaterials.net
https://doi.org/10.1016/j.xcrp.2025.102890

SUMMARY

Utilizing layered perovskites (LPKs) to passivate the surface of perovskite materials is a successful strategy that currently yields state-of-the-art record-breaking devices. Nevertheless, it is not clear what happens to the LPK once other layers are processed on top. Furthermore, these LPKs can provide benefits in both p-type-intrinsic-n-type (P-I-N) and its inverted n-type-intrinsic-p-type (N-I-P) perovskite solar cell configuration, despite significant differences in their processing. In this work, we propose that this occurs due to a convergent optimization pathway, due to the thinning down and dissolution of the LPK during the deposition of subsequent layers. Here, we use X-ray diffraction (XRD), scanning electron microscopy (SEM), and X-ray photoelectron spectroscopy (XPS) to demonstrate that for most of the “processing window” employed in the literature, the LPK is severely disrupted by the deposition of charge extraction layers. Indeed, the observation of highly crystalline layers via XRD correlates with a significant reduction in short-circuit current in solar cells, counteracting any other benefits.

INTRODUCTION

Contributing to the continuing success of perovskite solar cells is the widespread adoption of layered perovskite (LPK) passivation layers. This strategy is commonly described as leading to significant improvements in stability,[1–3] a minimization of recombination losses,[4] enhanced charge carrier extraction,[5] passivation of surface defects,[6,7] and improved band alignment.[8] The LPK has become a highly versatile treatment, improving device performance metrics irrespective of the system in which they are employed. Crucially, these improvements to performance occur despite the susceptibility to degradation of LPKs upon exposure to light, moisture, or fabrication solvents.[9–11]

However, despite 10 years of consistent optimization, no single deposition protocol has emerged as superior. In fact, seemingly widely different formulations, which *a priori* lead to very different LPK thicknesses, ultimately lead to a similar optimized efficiency value. Table 1 contains a representative selection of recipes utilized in the fabrication of high-performing solar cells in the literature. Both n-type-intrinsic-p-type (N-I-P) and p-type-intrinsic-n-type (P-I-N) cells employ LPKs, most commonly formed directly on top of the perovskite absorber layer, underneath the hole (N-I-P) or electron (P-I-N) extraction layer. For N-I-P cells, optimum performance is achieved with higher LPK-cation solution concentrations in the casting solution. These typically show the formation of highly crystalline layered phases detectable in X-ray diffraction (XRD) measurements. For P-I-N structures, the reverse is true, where lower concentrations yield optimum performance, with no detectable crystalline structures in XRD.

The improvements in performance occur across a range of different perovskite absorber recipes, with different band gaps and energy-level alignments (see Table 1). This raises questions about the role of the LPK—for example, which of the numerous reported benefits are truly at play within any given system? Complicating the picture is the fact that most reported characterization is carried out on perovskite bilayers, without depositing the charge extraction layers and/or the electrode contacts. This creates a disconnect between the sample studied and what is *actually* present in a device.

In this work, we seek to address this challenge by studying the impact of subsequent processing steps on the integrity of the LPK/perovskite heterojunction. We employ XRD, scanning electron microscopy (SEM), and X-ray photoelectron spectroscopy (XPS) to quantify the disruption of the LPK. Furthermore, we correlate device performance metrics to the crystallinity and integrity of the heterojunction that are present after fabrication is completed. Crucially, we find that the LPK is typically thinned down or eliminated altogether when employing state-of-the-art device fabrication conditions. Interestingly, this behavior occurs in both N-I-P and P-I-N devices, despite differences in the solution used for the subsequent layer deposition. This finding leads us to propose

Table 1. Selection of N-I-P and P-I-N solar cell compositions

Device architecture	Perovskite composition	Capping cation	Concentration at max PCE	Reference
N-I-P	$FA_{0.93}Cs_{0.07}PbI_3$	$DecA^+$	15 mM	Li et al.[3]
–	$FA_{0.92}MA_{0.08}PbI_3$	PEA^+	20 mM	Jiang et al.[7]
–	$FA_{0.85}MA_{0.1}Cs_{0.05}PbI_3$	PEA^+	20 mM	Petrulevicius et al.[12]
–	$Cs_{0.05}FA_{0.85}MA_{0.1}PbI_3$	$MeO\text{-}PEA^+$	16 mM	Du et al.[13]
–	$Cs_{0.1}(FA_{0.83}MA_{0.17})_{0.9}Pb(I_{0.83}Br_{0.17})_3$	$PEA^+F\text{-}PEA^+$	16 mM7.5 mM	Zhou et al.[14]
–	$FA_{0.95}MA_{0.05}PbI_{0.95}Br_{0.05}$	PEA^+	20 mM	Chen et al.[15]
P-I-N	$Cs_{0.03}(FA_{0.9}MA_{0.1})_{0.97}PbI_3$	OLA^+	1.25 mM	Azmi et al.[2]
–	$Cs_{0.05}(FA_{0.95}MA_{0.05})_{0.95}Pb(I_{0.95}Br_{0.05})_3$	PEA^+	4 mM	Xiong et al.[5]
–	$FA_{0.98}Cs_{0.02}PbI_3$	$PEA^+F\text{-}PEA^+$	4 mM3.7 mM	Chen et al.[6]
–	$Cs_{0.05}FA_{0.85}MA_{0.1}PbI_3$	PEA^+	4 mM	Chen et al.[15]
–	$FA_{0.93}MA_{0.02}Cs_{0.05}PbI_{2.94}Br_{0.06}$	PEA^+	4 mM	Zhou et al.[16]
–	$(FA_{0.98}MA_{0.02})_{0.95}Cs_{0.05}Pb(I_{0.98}Br_{0.02})_3$	OLA^+	2.5 mM	Zhao et al.[17]

"Concentration at max PCE" values are LPK-cation solution concentrations used for devices with the highest power conversion efficiency (PCE) using that cation in the work.

a convergent optimization pathway: N-I-P device recipes that use a thicker LPK "thin down" their LPK with the subsequent hole transport material (HTM) deposition. In contrast, P-I-N architectures use an initially thinner LPK and processing conditions that disrupt and recrystallize the layer to a lesser degree, reaching a similar final state of the LPK component.

RESULTS

XRD studies during device fabrication

To prove that characterizing an incomplete device can lead to a misleading understanding of the system, we performed XRD measurements on typical mixed-cation, mixed-halide N-I-P and P-I-N solar cells during various stages of fabrication. Figure 1 illustrates this process, with the corresponding X-ray diffractograms after the deposition of each of the layers that make up a full N-I-P (Figure 1B) and P-I-N (Figure 1D) solar cell. The bulk perovskite compositions in this work were selected to reflect the complex alloys used in champion N-I-P and P-I-N devices. The composition used in the N-I-P case was a $Cs_{0.05}MA_{0.1}FA_{0.85}PbI_3$ triple-cation perovskite, while the P-I-N case used a double-cation $Cs_{0.1}FA_{0.9}PbI_{2.87}Br_{0.13}$ composition.

As the layers that make up the solar cells are deposited, we observe the expected formation of the 3D perovskite with the characteristic peak at 14.1° (see Figures 1B and 1D, red curve). After the deposition of the LPK-cation solution, the characteristic (002) peak of an $n = 1$ LPK at 5.4° appears, as seen in the pink curve. Here, these layers were deposited using 15 mM solutions of phenylethylammonium iodide (PEAI) in isopropanol (IPA) and annealed after deposition. Figures S1A–S1F and S3A–S3F contain the data collected for films fabricated using concentrations from 0 to 50 mM, covering the full gamut of recipes, with wider-angle scans included in Figures S2 and S4. Once the charge extraction layer is deposited over the top of the LPK, this (002) peak vanishes in the N-I-P sample and is significantly reduced and broadened in the P-I-N sample, as seen in the green curves. This trend holds across all of the other concentrations studied (see Figures S1–S3). In fact, our data show that the LPK peak vanishes for all but the highest concentrations of LPK-cation solutions upon deposition of the charge transport layer. See Note S1 for additional discussion.

Identification of the LPK loss mechanism

To explore the mechanism behind these changes to the LPK peak, we carried out a combined XRD and SEM study on N-I-P and P-I-N perovskite-LPK bilayers. Next, the HTM/electron transport material (ETM) for each architecture was separated out into its key "components" and then deposited on the bilayer to identify what is responsible for the sharp loss in LPK peak intensity. The XRD data in Figure 2A show that the behavior of the N-I-P system reflects the measurements on actual devices—after deposition of doped Spiro-OMeTAD, the LPK peak is no longer visible. However, if the Spiro is not doped, the LPK peak remains, with a reduced intensity. Finally, we washed the LPK with a dopant-only HTM solution using the same solvent combination used in state-of-the-art Spiro-OMeTAD deposition protocols.[3,12,13] This "HTM wash" consists of chlorobenzene (CB) mixed with *tert*-butyl pyridine (tBP), lithium bis(trifluoromethanesulfonyl)imide (Li-TFSI), and FK209 cobalt(III)-TFSI salts dissolved in acetonitrile (ACN). Here, we observe both a reduction of the initial LPK peak and the growth of an additional peak at around 4°, associated with an $n = 2$ phenylethylammonium (PEA)-based LPK.[18]

SEM images corresponding to the XRD data are shown in Figures 2B–2F. Initially, we observe smooth, wave-like features on the grain surface, which we identify as the LPK conformally growing over the underlying perovskite (Figure 2C). These features vanish entirely after the deposition of doped Spiro-OMeTAD (Figure 2D) but are still present if undoped Spiro is used (Figure 2E). We note that to allow us to image the perovskite surface after HTM deposition, we removed the Spiro films with a CB rinse. We confirm that CB on its own does not significantly disrupt the LPK (shown in Figures S5 and S6). Diffractograms of the intact Spiro and CB-washed films are shown in Figure S7. Finally, in the case of the HTM wash dopant-only sample, we observe clear evidence of recrystallization of the top LPK layer into small, plate-like domains. These platelets are

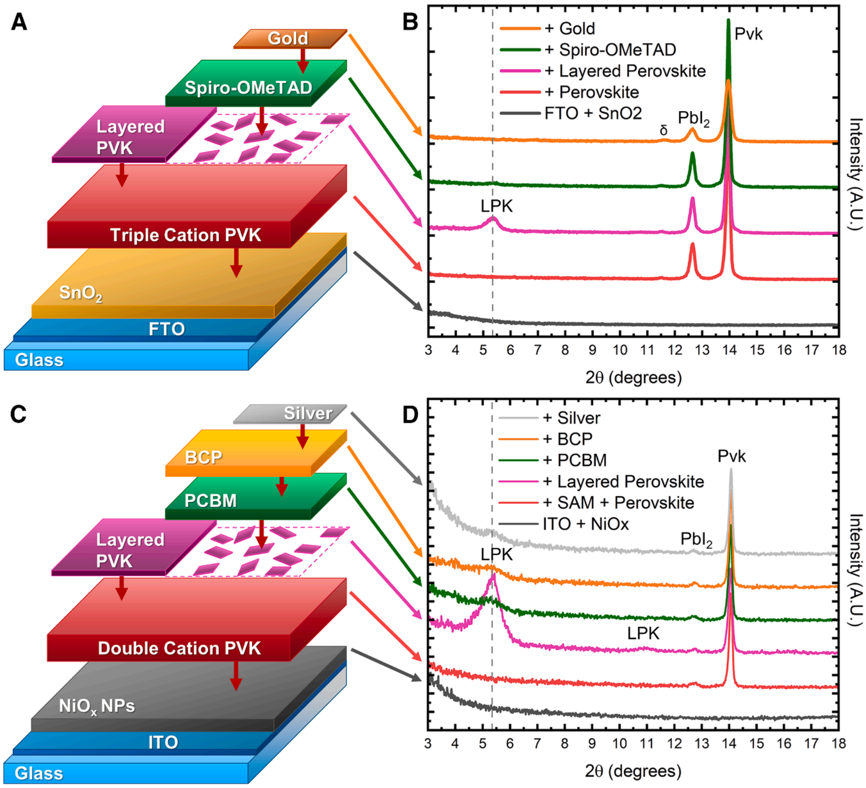

Figure 1. Study of LPK integrity throughout device fabrication

Illustration of the sequential deposition of the layers making up an N-I-P (A) and P-I-N (C) solar cell, with the corresponding XRD diffractograms of N-I-P (B) and P-I-N (D) perovskite solar cells after the deposition of each layer during fabrication. Peak labels identify the corresponding crystalline phase, with the position of the (002) $n = 1$ layered perovskite peak indicated by the dashed line. For studies of additional compositions, see Figures S1–S4.

disconnected from the underlying perovskite, often spanning grain boundaries (highlighted in Figure S8).

In the P-I-N system (Figure 3), we observe the same behavior in the XRD data as in the initial device study. Here, the deposition of (6,6)-phenyl C61 butyric acid methyl ester (PCBM) results in a significant reduction in intensity and broadening of the LPK peak. As there are no dopants in the PCBM solution, we instead “broke up” the molecule into two parts: the fullerene modeled by C_{60} and the ester tail modeled by methyl pentanoate (MPA). Both components were dissolved in CB at a concentration of 20 mg/mL and resulted in a similar reduction in the LPK peak intensity. The SEM images (Figures 3B–3F) show less obvious disruption to the surface LPK layer for all cases. The wave-like features indicating conformally grown LPK are still clearly present in the washed PCBM and C_{60} samples. Washing the perovskite with a solution containing MPA in CB results in corrugation of the surface. This indicates partial dissolution of the surface, albeit to a much smaller extent than what was observed for the HTM wash sample shown in Figure 2.

The combination of XRD and SEM data for the two systems leads us to propose the following mechanisms for the loss of crystalline LPK after HTM/ETM deposition (illustrated in Figure 4). In P-I-N architectures (Figure 4A), the deposition of small molecules thins down the LPK via a combination of physical ablation and a small degree of dissolution. We note that this combined disruption may be less prominent if the ETM is deposited via chemical vapor deposition (CVD) or other techniques that do not rely on solution processing of the material.

In the case of N-I-P structures (Figure 4B), doping the HTM requires adding polar solvents such as ACN or tBP. Even in small quantities, these can dissolve the deposited LPK, either washing it off entirely or causing it to be recrystallized into disconnected platelets. This, combined with any mechanical ablation effects that may be present, acts to severely disrupt the LPK, often removing it from the surface of the material entirely.

Impact of LPK processing conditions

To generalize our findings, we explored the behavior of alternate LPK compositions deposited at a range of concentrations, with and without annealing steps. We applied the dopant-only HTM wash approach and performed XRD, SEM, and XPS measurements to track the impact of the HTM solvent system on LPK loss and dissolution.

The XRD diffractograms, shown in Figures S9 and S10, clearly demonstrate that the solvents contained within the HTM wash recrystallize the surface LPK material. For PEAI deposited at low concentrations, this means that the LPK peak is no longer visible, while for higher concentrations, we observe peaks corresponding to the $n = 1$ and 2 LPK phases remaining on the surface. Samples prepared without annealing behave in the same manner. While initially, they contain co-crystallized LPK-cation salt at lower LPK concentrations, it is lost after the HTM wash, and a higher LPK concentration in the casting solution (20 mM) is required for a peak to remain visible.

SEM images, shown in Figures S11 and S12, give further evidence for the recrystallization of the LPK. For all concentrations where conformal LPK growth is observed, the HTM wash results in the formation of disconnected platelets on the perovskite surface. The quantity of these increases alongside the initial LPK concentration, and it is higher if the LPK was annealed after deposition. The degree of surface coverage of the remaining platelets differs significantly between the annealed and unannealed samples. With annealing, platelets cover approximately 76% and >95% of the surface for the 15 and 50 mM samples, respectively. In the unannealed case, these values are approximately 0% and 46%, respectively. Figures S13 and S14 show false-color images of two of the samples that were used to quantify these values. In each case, if platelets are observed after the HTM wash, there is an LPK peak visible in the XRD data. This

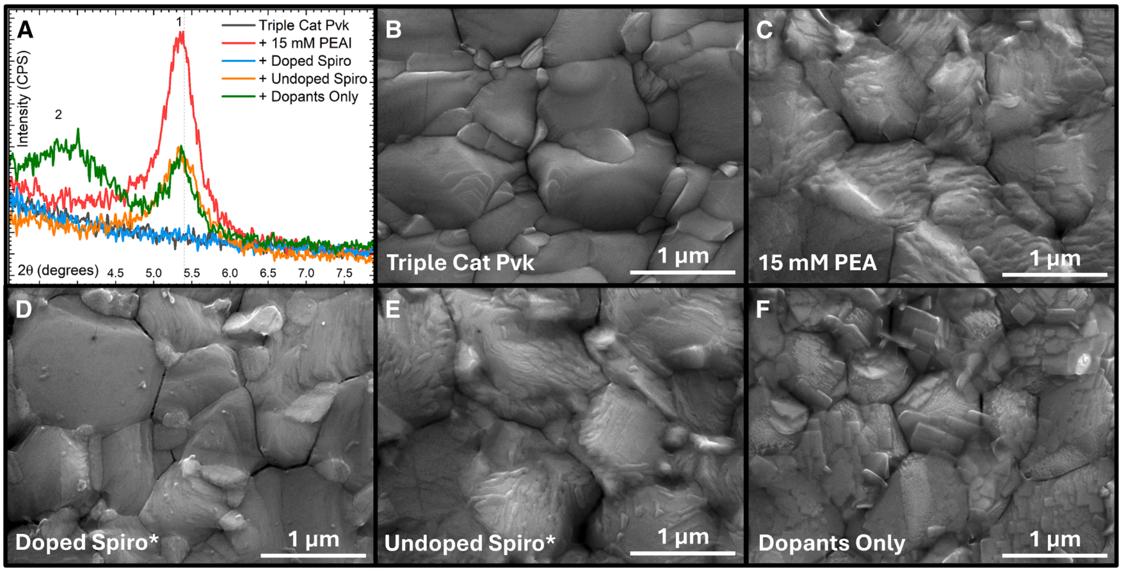

Figure 2. Identifying the mechanism of LPK loss in N-I-P devices

XRD diffractograms of the (002) LPK peaks (A) and corresponding SEM images (B–F) after deposition of various HTM components.

(B) A reference triple-cation perovskite film.

(C) A triple-cation perovskite film coated with 15 mM of PEA cation solution.

(D) The 15 mM film after depositing Spiro-OMeTAD, following a CB rinse.

(E) The 15 mM film after depositing undoped Spiro-OMeTAD, following a CB rinse.

(F) The 15 mM film after a dopant-only HTM wash. The scale bars represent 1 μm.

offers strong evidence that the observed platelets in the SEM images correspond to the recrystallized LPK.

We further investigated whether 4-fluoro phenylethylammonium iodide (F-PEAI) undergoes a similar disruption after HTM deposition. This cation is often utilized as a “more stable” alternative to the PEAI salt, and it is an excellent candidate for state-of-the-art devices.[14] The XRD diffractograms and SEM images, included in Figures S15 and S16, respectively, show that the F-PEAI cation is indeed more stable when treated with the HTM wash. We observe a lower loss of LPK peak intensity in the XRD data, in contrast to the data presented in Figures S9 and S10 for PEAI. SEM images of the sample surface show regions of platelet formation alongside the initially deposited LPK, demonstrating that even this more stable cation undergoes some degree of dissolution.

These results conclusively demonstrate the severe impact the HTM solvent can have on the LPK. The SEM images prove that whatever material remains is structurally different from the initially present layer, losing good coverage and conformal growth on the underlying perovskite grains. This must be taken into consideration when discussing the impact and behavior of the LPK in a device. At the LPK-cation concentrations most widely employed in the literature, it is highly unlikely that it acts as a uniform barrier preventing direct contact between the HTM/ETM and the bulk material underneath, as is commonly illustrated.[19–21]

Phase identification via XPS

In order to gain further insights into the disruption of the LPK-perovskite heterojunctions during the HTM/ETM deposition, we carried out XPS measurements. This allows us to corroborate the observed changes in LPK coverage as determined by SEM and XRD. This technique characterizes the species present within the first few nm of the perovskite film, giving information on the composition of the layers forming the heterojunction. Here, four representative LPK-cation concentrations were chosen, corresponding to an uncoated triple-cation perovskite sample, one with a very thin LPK (2.5 mM), one with a high quantity of LPK (15 mM), and one with co-crystallized PEA cation (50 mM). In all cases, the LPK was annealed after deposition.

Figure 5A shows the C 1s spectra of films with as-formed LPK heterojunctions. Assignments of carbon-bonding environments were carried out by comparing the binding energy separations between sample peaks and reference cation powders (see Table S4). As the amount of LPK is increased, we observe a reduction of the carbon peak at 288.7 eV, associated with the N=C–N bond present in the formamidinium cation. For the 50 mM sample, this peak is indistinguishable from the baseline. Alongside this, we observe the growth of the broad aromatic π–π^* satellite peak centered around 293 eV and the C–NH_3 peak at 286.6 eV. This is compelling evidence of the buildup of PEA on the perovskite surface, corroborating our XRD data. The Cs 3d spectra shown in Figure 5B show that the signal is not detected in the 50 mM sample. This means that the thickness of the material deposited is above the probed depth of the XPS measurements of around 8.7 nm, proving a complete coverage of the perovskite surface. This was determined by calculating the inelastic mean free path (IMFP; λ) using the Pb 4f signal and the Tanuma, Powell, and Penn TPP-2M formula as implemented in the NIST software.[22,23] According

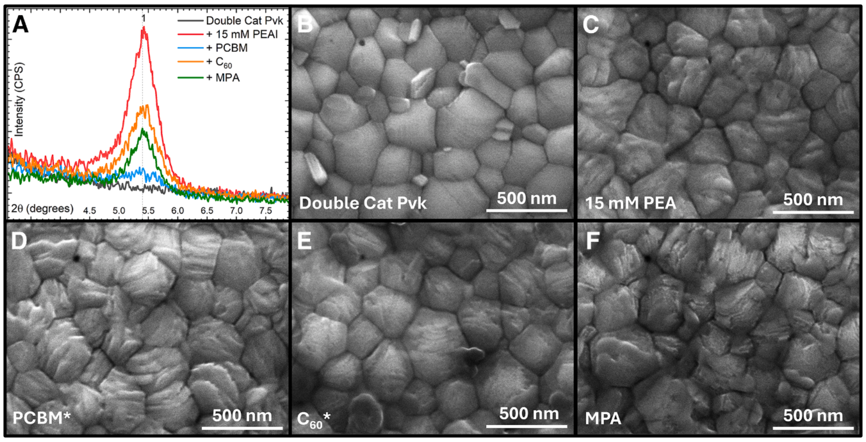

Figure 3. Identifying the mechanism of LPK loss in P-I-N devices

XRD diffractograms of the (002) LPK peaks (A) and corresponding SEM images (B–F) after deposition of various ETM components.

(B) A reference double-cation perovskite film.

(C) A double-cation perovskite film coated with 15 mM of PEA cation solution.

(D) The 15 mM film after depositing PCBM, following a CB rinse.

(E) The 15 mM film after depositing C_{60} following a CB rinse.

(F) The 15 mM film after washing with MPA in CB.

The scale bars represent 500 nm.

to the Beer-Lambert law, 67% of the XPS signal is from λ = 2.9 nm, whereas about 95% of the XPS signal is from 3λ = 8.7 nm.[24] Full XPS data, including fitted C 1s regions, reference powder data, and tables listing all peak positions, are included in the supplemental information (Figures S17–S19; Tables S1–S4). Sample degradation in the instrument was minimal, with no observation of the formation of $Pb^{(0)}$ during measurement, as shown in Figure S20.

Comparing the initial spectra to those with an HTM wash, shown in Figures 5C and 5D, we observe that the 288.7 eV FA^+ peak is clearly visible in all films, with an essentially equivalent intensity for all films. In the 50 mM case, the C–NH_3 peak is still visible at 286.6 eV, and the C–C 285 eV peak is far more intense, suggesting that there still is some LPK present. The new peak located at 293.5 eV is the C–F_3 group of the TFSI anion dissolved in the HTM wash, which was deposited on the surface during the washing step.[25] In the Cs 3d spectra in Figure 5D, we now observe a Cs 3d peak for all LPK-cation concentrations used, indicating that the LPK or co-crystallized LPK-cation salt is no longer fully covering the 3D perovskite at the 50 mM concentration, as in Figure 5B. This may be due to either a thinning of the LPK or a non-uniform etch where parts of the LPK are removed, creating incomplete coverage. The latter would lead to regions of both layered and 3D perovskite exposed to the incident X-ray beam, and thus both signals would be present in the spectra. Both mechanisms can occur in tandem and would be consistent with the XRD and SEM evidence indicating the ablation or dissolution of the LPK and the formation of platelets on the 3D perovskite surface.

Taken together, the XRD, XPS, and SEM studies offer unequivocal evidence that passivation layers of low-dimensional perovskites undergo a pronounced dissolution and recrystallization during the HTM deposition process, with the resulting structure differing significantly from its common description of a "uniform passivation layer."[26,27] Indeed, for a significant portion of the processing window employed in the literature, the layered structure is fully lost. In these cases, we propose that the residual organic cations serve to passivate surface traps and are likely localized on defect-prone regions of the material, such as grain boundaries. This hypothesis is corroborated by recent work by Cacovic et al., who used spatial mapping techniques to demonstrate that a reduction of non-radiative recombination can occur when using very low (0.5 mM) LPK-cation solution concentrations.[28]

Correlating LPK quantity with optimal device performance

To further explore the impact of the disruption of the LPK in solar cells, we prepared a series of P-I-N (indium-doped tin oxide [ITO]/NiOx/double-cation perovskite/LPK/PCBM/bathocuproine [BCP]/Ag) and N-I-P (fluorine-doped tin oxide [FTO]/SnO_x/triple-cation perovskite/LPK/Spiro-OMeTAD/Au) devices. Here, the LPK-cation concentration range was chosen to match our characterization studies. For P-I-N cells, the LPK layer was subject to an annealing step after fabrication, while for N-I-P cells, LPK was left unannealed, as is standard in champion device recipes.[12,15]

Representative devices have been plotted in Figure 6, with the full device performance metrics provided in Tables S5 and S6 and Figures S21 and S22. Here, the results show that all devices that include an LPK see an increase in open-circuit voltage (V_{OC}) with more concentrated LPK-cation solutions, rising from 1.09 ± 0.01 V for plain perovskite samples up to 1.13 ± 0.01 V for 20 mM. In P-I-N cells, this rise in V_{OC} occurs alongside a significant reduction in the short-circuit current (J_{sc}) once a threshold concentration of 4 mM is passed. In contrast, N-I-P cells demonstrate a far smaller variation in J_{SC} across the same concentration range. Only if the LPK-cation concentration is taken up to 50 mM do we observe a similar reduction in J_{SC}. We note that if we anneal the LPK in N-I-P cells, we observe a similar sharp reduction in J_{SC}, as shown in Figures S23 and S24 and Table S7.

Interestingly, despite significant differences across the full fabrication process for both N-I-P and P-I-N devices, the optimum LPK-cation concentration corresponds to those where the LPK is no longer detectable in XRD measurements (see Figure S25). We propose that this convergent optimization of the LPK/perovskite heterojunction occurs due to the complex interplay between the processing steps throughout the solar cell fabrication. For N-I-P devices, the HTM casting solution contains numerous additives that disrupt any formed LPK. Furthermore, optimized recipes usually avoid annealing the deposited LPK,[7,12] which leads to a more co-crystallized LPK-cation salt

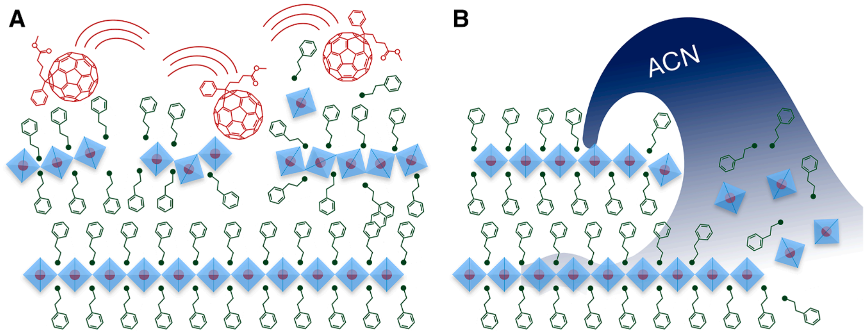

Figure 4. Proposed mechanisms for the loss of LPK after charge transport material (CTM) deposition

(A) Physical ablation of the surface during the deposition of small-molecule ETMs in non-polar solvents.

(B) Washing of the surface during the deposition of HTMs that require the addition of polar solvents.

and less LPK in the sample. This, in turn, makes the layers more susceptible to washing by the polar solvents present in the HTM. In contrast, P-I-N cells most commonly anneal the LPK and either use ETM molecules directly dissolved in an organic solvent or forgo a solution processing step entirely. This means that ETM deposition disrupts the LPK to a lesser degree.

In essence, we find that the optimal LPK-cation concentration in P-I-N devices is far lower than for N-I-P cells, reflecting the optimized device recipe trends in the field as a whole, as listed in Table 1. This point is illustrated in recent work by Chen et al.[15] In their work, optimized N-I-P cells use a 5 times higher PEA solution concentration than the P-I-N cells, and using the same high concentration for both architectures leads to significant current losses in the P-I-N cell, similar to the results presented in Figure 6. Overall, our data suggest that LPK platelets past an estimated lower bound of 3 layers are already too thick and limit the device performance—for a derivation of this value, calculated for a widely available benchtop XRD instrument employing a fast scan, see Note S2 and Figures S26 and S27.

DISCUSSION

Identifying that LPK passivation is unlikely to remain as a distinct layer within the material raises an important question regarding the mechanism by which these layers improve the long-term stability of perovskite solar cells. Effects such as increased hydrophobicity, which is often demonstrated on partial bilayers, are likely far less pronounced and potent in the completed device.[6] Instead, we propose that the key role LPKs play is in passivating surface defects and shallow trap states.[29] Such defects reduce the activation energy barriers, leading to large-scale degradation, reducing perovskite stability.[30] Indeed, surface defects have been demonstrated to be key sites in mediating moisture-, oxygen-, and light-induced degradation.[31]

Finding pathways to limit the degree of disruption of the LPK could help reduce the gap between our understanding of the impact of an initially formed material and what is present in the cell after fabrication. As the F-PEAI cation was demonstrated to be more resilient to dissolution, depositing cations with stronger intermolecular interactions, utilizing materials that can be crosslinked after deposition, or exploiting more robust 1D perovskite alternatives should act to limit the damage to the initially formed LPK.[32,33] Alternatively, focusing on dopant-free CTM molecules and avoiding solution processing may lead to similar reductions in LPK losses.

Finally, we would like to highlight an important issue in comparing LPK deposition protocols across different research groups. Variations in the deposition technique and post-processing of the layers can lead to significant differences in what is ultimately present in the solar cell. To illustrate this, we have prepared a series of samples incorporating LPKs deposited from a 15 mM LPK-cation solution with a range of spincoating protocols, as shown in Figure S28. The data unambiguously demonstrate that for a given LPK-cation solution concentration, a significant variation in the intensity of the (002) LPK peak in the resulting film is observed through XRD measurements. This high potential for group-to-group variation with nominally the same recipe highlights the need for a thorough characterization of actual as-fabricated devices, rather than simple bilayers, for an accurate understanding of any experiments carried out on LPK systems.

In this work, we identify that the deposition of charge transport layers causes significant disruption to LPKs utilized as passivation layers in typical perovskite solar cells. XRD studies during the fabrication of P-I-N and N-I-P devices show that initially crystalline LPKs are lost upon completing the solar cell for all but the thickest of layers. Furthermore, by isolating the components making up the charge transport layer solutions, we elucidate the mechanism by which this process occurs, namely, a combination of dissolution and ablation. We find that in a P-I-N configuration, the ETM molecules themselves damage the LPK, while in N-I-P architectures, polar solvent additives can act to dissolve the LPK. Indeed, our results clearly show that initially, conformally grown LPKs are either washed off entirely or redistributed into a network of disconnected platelets. This reduces the quantity and coverage of the LPK material on the perovskite surface.

Nevertheless, disrupted LPKs still achieve their function for improving solar cell performance compared to devices that do not include them. However, we find that the presence of clearly identifiable crystalline LPK in XRD measurements correlates with a significant drop in power conversion efficiency for both P-I-N and N-I-P devices. Instead, our results show that platelets between 3 and 5 nm thick are optimal for device performance. To achieve this condition, P-I-N and N-I-P devices have developed a convergent optimization strategy. More aggressive solvent systems typically employed in N-I-P fabrication are compensated for by using initially thicker LPKs, whereas the less aggressive P-I-N solvent systems start from a thinner LPK. Thus, the recipes reach the same final structure.

Our work unambiguously demonstrates that the characterization of partial bilayers of perovskite is not representative of the

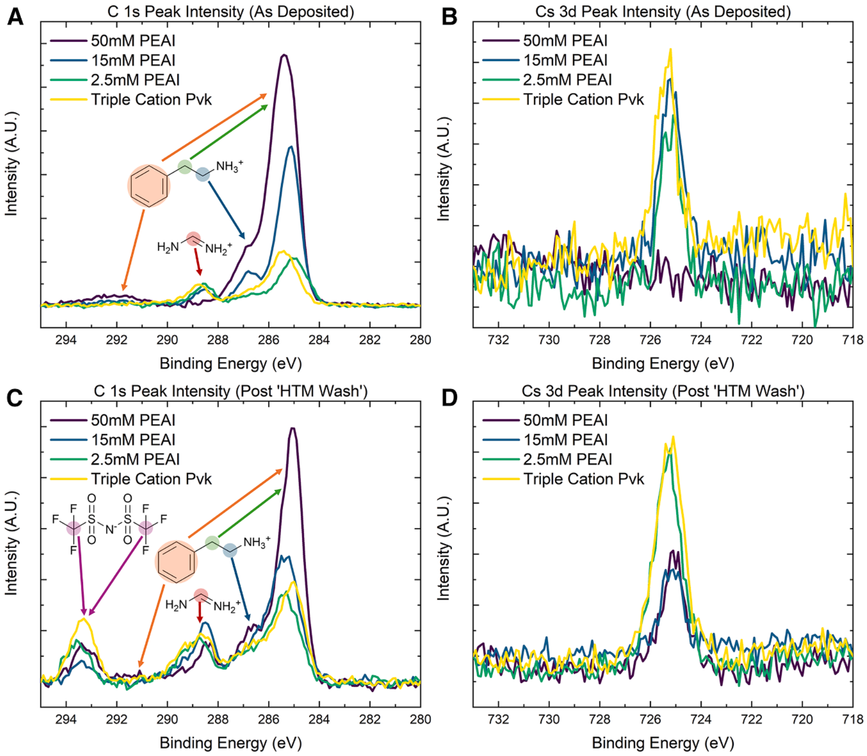

Figure 5. Baseline-subtracted XPS spectra of LPK-perovskite heterojunction films

(A) C 1s region of as-deposited films.

(B) Cs 3s region of as-deposited films.

(C) C 1s region of films after the HTM wash.

(D) Cs 3s region of films after an HTM wash.

Figures S17–S19 contain the peak fitting for the C 1s regions, with peak position information included in Tables S1–S4.

system found within full devices. Indeed, we believe that this disconnect between what is assumed to be in the device and what is *actually* in the device has hampered progress. For representative results, it is key to measure *in situ* and use samples that account for the impact of any further fabrication steps.

METHODS

Synthesis of organic salts

Unless stated otherwise, all chemicals were purchased from commercial sources and used without further purification. MAI and PEAI precursors used were synthesized in our laboratory, as reported in our other work.[9] For the fabrication of P-I-N devices, PEAI was purchased from GreatCell Solar.

NiOx nanoparticle synthesis

In a fumehood, 6 g of $Ni(NO_3)_2{\cdot}6H_2O$ (Duksan) was dissolved in 80 mL of deionized (DI) water under vigorous stirring until a clear solution was obtained. Subsequently, 80 mL of 1 M NaOH (97%, Alfa Aesar) solution (1 mol/L in DI water) was added dropwise at a controlled rate. The mixture was stirred continuously for 5 min. The resulting light-green precipitate was collected via centrifugation at 10,000 rpm and washed several times with DI water. The purified product was then freeze dried for at least 48 h before being annealed at 270°C for 2 h, yielding black NiO_x nanoparticles.

P-I-N solar cell fabrication

Pre-patterned ITO substrates were sequentially cleaned by using a 1% Decon 90 solution in DI water, followed by DI water, acetone, and ethanol by sonication for 15 min in each solvent. The cleaned substrates were then dried with nitrogen gas and treated with oxygen plasma at 10 V for 10 s (Spectrolinker XL 15000). For the hole transport layer, an NiOx nanoparticle ink (20 mg/mL in DI water) was spin coated onto the ITO surface at 4,000 rpm for 30 s inside a fumehood. The coated substrates were then annealed at 110°C for 10 min, followed by UV-ozone treatment for 20 min before being transferred to a nitrogen-filled glovebox. A solution of 0.5 mg/mL Me-4PACz (99%, TCI) in IPA (99.8%, Alfa Aesar) was spin coated at 4,000 rpm for 30 s and annealed at 100°C for 10 min. The perovskite precursor solution was prepared by dissolving 450 mg of PbI_2 (>99.9%, TCI), 155 mg of formamidinium iodide (FAI) (GreatCell Solar), 26 mg of caesium iodide (CsI) (>99%, TCI), and 24 mg of lead (II) bromide ($PbBr_2$) (>99.9%, TCI) in 571 μL of dimethylformamide (DMF) (99.8%, Alfa Aesar) and 143 μL of dimethyl sulfoxide (DMSO) (99.7+%, Alfa Aesar). The solution was heated at 60°C overnight and filtered before use. The perovskite film was formed using a two-step spin-coating process: first at 2,000 rpm for 10 s and then at 4,000 rpm for 30 s. During the final 10 s of the second step, 250 μL of CB (>99.5%, Aladdin) antisolvent was added. The perovskite films were then annealed at 100°C for 30 min. After annealing, a PEAI (GreatCell Solar) solution (1-20 mM) in IPA was applied for 5 s, followed by spin coating at 5,000 rpm for 30 s and an additional annealing step at 100°C for 3 min. For the electron transport layer, a PCBM (>99.8%, Lumtec) solution (20 mg/mL in CB) was spin coated at 1,200 rpm for 30 s, followed by an additional annealing at 100°C for 10 min. The BCP (>99.5%, Lumtec) layer (1 mg/mL in IPA) was deposited by spin coating at 4,000 rpm for 30 s. A 90-nm-thick silver (99.99%, Kurt J. Lesker) electrode was thermally evaporated through a shadow mask, defining an electrode area of 0.09 cm^2. The completed devices were encapsulated using microscope glass and polyisobutylene tape, with edges sealed using UV-cured epoxy. To measure the performance of the devices, J-V measurements were carried out using a Keithley 2400 source measure unit under 1 sun illumination (100 mW/cm^2) with an AM1.5G spectrum. An ABET Sun 2000 solar simulator was calibrated with an Enli PVM silicon standard reference cell. The measurements were conducted in ambient conditions

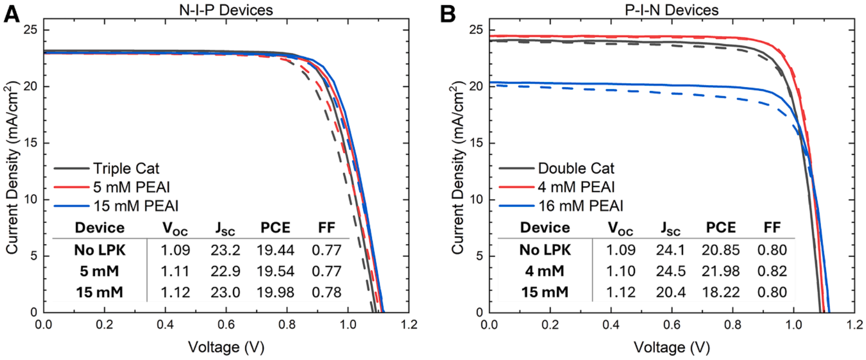

Device	V_{OC}	J_{SC}	PCE	FF
No LPK	1.09	23.2	19.44	0.77
5 mM	1.11	22.9	19.54	0.77
15 mM	1.12	23.0	19.98	0.78

Device	V_{OC}	J_{SC}	PCE	FF
No LPK	1.09	24.1	20.85	0.80
4 mM	1.10	24.5	21.98	0.82
15 mM	1.12	20.4	18.22	0.80

Figure 6. Best-performing solar cell data
N-I-P (A) and P-I-N (B) architecture cells fabricated with increasing concentrations of PEAI cation solution. Champion device performance for the full dataset is included in Tables S5 and S6. Statistical breakdowns of device performance are included in Figures S21 and S22.

(room temperature, relative humidity of 50%–60 %) using an aperture mask of 0.04 cm^2. The reverse scan was performed from 1.2 to −0.2 V with a step of 0.03 V and a delay of 10 ms, and the forward scan was conducted from −0.2 to 1.2 V.

N-I-P solar cell fabrication

FTO glass substrates were chemically patterned using a mixture of Zn powder (>99.99%, Sigma-Aldrich) and 3 M hydrochloric acid (Sigma-Aldrich) and then cleaned sequentially using Hellmanex III, DI, acetone (VWR), ethanol (VWR), and DI water. The ETM was prepared via a chemical bath deposition procedure in a water bath heated to 90°C for 4.5 h inside a fumehood. The precursor solution was prepared by mixing 412.5 mg $SnCl_2 \cdot 2H_2O$ (>99.99%, Sigma-Aldrich), 1.875 g urea (99%, Sigma-Aldrich), 1.875 mL HCl (37%, Sigma-Aldrich), and 37.5 μL thioglycolic acid (>99%, Sigma-Aldrich) in 150 mL DI water. After deposition, the substrates were sonicated in DI water and isopropyl alcohol for 5 min each and dried at 100°C for 1 h. The substrates were then annealed at 190°C for 1 h and treated with UV-ozone (Ossila) for 30 min. Substrates were then transferred to a nitrogen-filled glovebox before perovskite deposition. The perovskite precursor solution contained 0.07 M CsI (99.999%, Sigma-Aldrich), 0.08 M MAI, 1.32 M FAI (>99%, Sigma-Aldrich), 0.5 M MACl (>99%, Sigma-Aldrich), and 1.54 M PbI_2 (>99.9%, TCI) in a mixed DMF (99.8% Extra Dry, Thermo Scientific) and DMSO (99.7+% Extra Dry, Thermo Scientific) solution with a volume ratio of 4:1. From this, 50 μL was spin coated onto the substrates at 1,000 rpm for 10 s and 4,000 rpm for 40 s. In the last 5 s, 250 μL of ethyl acetate (99.9% Extra Dry, Thermo Scientific) was dropped on the films. The perovskite films were then annealed at 100°C for 60 min and 150°C for 10 min. Next, 50 μL of a PEAI solution in IPA (99.8%, Thermo Scientific), ranging from 1 to 50 mM, was deposited on the slides. 5 s after deposition, the solution was spun off at 5,000 rpm for 30 s. An optional annealing step was carried out at 70°C for 10 min. For the hole transport layer, a 80 mg/mL Spiro-OMeTAD (99%, Sigma-Aldrich) solution in CB (99.8% Extra Dry, Thermo Scientific) was doped with 23 μL of LiTFSI (>99.9% anhydrous, Sigma-Aldrich) stock solution (520 mg in 1 mL ACN [>99.9%], Sigma-Aldrich), 14 μL of FK-209 (cobalt(III) salt) stock solution (375 mg in 1 mL ACN), and 32 μL of tBP (98%, Sigma-Aldrich) prior to spin coating. 50 μL of the HTM solution was then spin coated onto the perovskite at 3,000 rpm for 30 s. Samples were then moved to a desiccator and allowed to oxidise for 24 h. Finally, a 50-nm-thick gold (99.99%, Tesbourne) electrode was thermally deposited through a shadow mask, defining an electrode area of 0.16 cm^2. Devices were then sealed using a sealing tape (Helioseal PVS 101). J-V measurements were carried out using an Ossila source meter unit and a Wavelabs Sinus-70 AAA solar simulator with 1 sun (AM1.5G) illumination, calibrated using a Fraunhofer ISE calibration diode, and referenced to an AMS Osram BPW 34 silicon diode to monitor drift. The measurements were conducted in ambient conditions (room temperature, relative humidity of 30%–40 %). The illuminated cell area was defined using an aperture mask of 0.125 cm^2. The forward scan was performed from 1.3 to −0.1 V at a rate of 0.2 V/s and a delay of 10 μs after holding the cells at 1 sun and 1.2 V for 10 s, and the reverse scan was conducted from −0.1 to 1.3 V.

Characterization sample fabrication

ITO or FTO glass substrates were cleaned sequentially using Hellmanex III, DI water, acetone, ethanol, and DI water, followed by a UV-ozone treatment (Ossila) for 15 min in a fumehood. Double- or triple-cation perovskite and LPK deposition was carried out inside a glovebox, according to the protocol for P-I-N or N-I-P solar cells, respectively, as described above. Unless stated otherwise, samples were annealed after LPK deposition. HTM solvent was prepared by mixing 23 μL of LiTFSI stock solution (520 mg in 1 mL ACN), 14 μL of FK-209 (cobalt(III) salt) stock solution (375 mg in 1 mL ACN), and 32 μL of tBP in 1 mL of CB. HTM-washed samples had 50 μL of the HTM solution spin coated on top at 3,000 rpm for 30 s.

XRD

XRD diffractograms were taken on a Rigaku Miniflex benchtop diffractometer, which used unfiltered Cu Kα radiation. For studies of cells during fabrication, samples were moved between the diffractometer and the glovebox after the deposition of each layer.

SEM

SEM images were taken on a TESCAN Clara S8152 instrument, operated at an acceleration voltage of 15 keV, with a 300 pA beam current. Samples were grounded to the Al stubs using silver paint and were left uncoated.

XPS

XPS spectra were collected on a Kratos Analytical AXIS Supra+, using an Al Kα (1,486.6 eV) excitation source. No charge neutralizer was used for thin-film samples. For reference powder samples, the charge neutralizer beam was set to 0.45 A, with a 1 V filament bias and a 4 V charge balance. Thin-film samples were grounded using copper tape and had gold contacts evaporated on top to ensure good electrical contact between the sample, mounting bar, and instrument. Surface photovoltage effects were minimised by keeping the sample in the dark during measurement, by turning off the instrument lighting and blocking off window ports. Samples were kept in a nitrogen atmosphere during preparation and transferred into the instrument via an air-free transfer mechanism to avoid exposure to ambient conditions. The chamber pressure was between 8.3E−8 to 1.3E−7 Torr during measurement. Curve fitting was performed using Igor Pro software with an XPS extension (XPST) coded, as described by Schmid et al.[34] The background for the peaks was different depending on the region and core levels and consisted of a simple linear background (e.g. Cs 3d core level) or a Shirley function (e.g. Pb 4f). The peak line shape implemented in the software used a Gaussian-Lorentzian sum function to approximate a Voigt profile, as explained in Schmid et al.[34] Gaussian-Lorentzian ratios were optimized between 0.3 (e.g C 1s and Cs 3d core levels) and 0.5 (e.g. O 1s level) as an iterative processm as described by Major et al.[35] For core levels showing multiple components, peak fitting was performed using the minimum number of peaks necessary to minimize the residual between the experimental data and the envelope, and each peak was assigned to a chemical state. For the Pb 4f levels, a doublet was fitted to reproduce the spin orbit (SO) splitting, with a binding energy separation of 4.88 eV and a ratio of 0.75 between the two SO components.

RESOURCE AVAILABILITY

Lead contact

Requests for further information and experimental data should be directed to the lead contact, Pablo Docampo (pablo.docampo@bcmaterials.net).

Materials availability

The study did not generate new, unique reagents.

Data and code availability

- All experimental data supporting this article have been included as part of the supplemental information.
- The custom code used to analyze solar cell data will be shared by the lead contact upon request.
- Any additional information required to re-analyze the data reported in this paper is available from the lead contact upon request.

ACKNOWLEDGMENTS

P.D. acknowledges support by the Engineering and Physical Sciences Research Council (EP/T010568/1). E.A. also acknowledges support by the Engineering and Physical Sciences Research Council (EP/X032116/1). G.C. thanks the Leverhulme Trust for a Research Fellowship. A.B.D. acknowledges support from RGC CRF project 7018-20G and Research Output Award of the University of Hong Kong.

AUTHOR CONTRIBUTIONS

Conceptualization, M.G. and P.D.; formal analysis, M.G. (lead) and E.A.; investigation, M.G. (lead), W.K.Y., M.M., and E.A.; methodology, M.G. and P.D.; resources, B.V. and J.W.; software, F.J.A.; supervision, P.D. (lead), G.C., and A.B.D.; visualization, M.G.; writing – original draft, M.G.; writing – review & editing, M.G., F.J.A., A.B.D., G.C., E.A., and P.D. (lead).

DECLARATION OF INTERESTS

The authors declare no competing interests.

SUPPLEMENTAL INFORMATION

Supplemental information can be found online at https://doi.org/10.1016/j.xcrp.2025.102890.

Received: April 1, 2025
Revised: June 25, 2025
Accepted: September 14, 2025
Published: October 6, 2025

REFERENCES

1. Grancini, G., Roldán-Carmona, C., Zimmermann, I., Mosconi, E., Lee, X., Martineau, D., Narbey, S., Oswald, F., De Angelis, F., Graetzel, M., and Nazeeruddin, M.K. (2017). One-Year Stable Perovskite Solar Cells by 2D/3D Interface Engineering. Nat. Commun. *8*, 15684. https://doi.org/10.1038/ncomms15684.
2. Azmi, R., Ugur, E., Seitkhan, A., Aljamaan, F., Subbiah, A.S., Liu, J., Harrison, G.T., Nugraha, M.I., Eswaran, M.K., Babics, M., et al. (2022). Damp Heat – Stable Perovskite Solar Cells with Tailored-Dimensionality 2D/3D Heterojunctions. Science *376*, 73–77. https://doi.org/10.1126/science.abm5784.
3. Li, J., Jin, C., Jiang, R., Su, J., Tian, T., Yin, C., Meng, J., Kou, Z., Bai, S., Müller-Buschbaum, P., et al. (2024). Homogeneous Coverage of the Low-Dimensional Perovskite Passivation Layer for Formamidinium–Caesium Perovskite Solar Modules. Nat. Energy *9*, 1540–1550. https://doi.org/10.1038/s41560-024-01667-8.
4. Mozaffari, N., Duong, T., Shehata, M.M., Bui, A.D., Pham, H.T., Yin, Y., Mayon, Y.O., Zheng, J., Mahmud, M.A., Tabi, G.D., et al. (2022). Above 23% Efficiency by Binary Surface Passivation of Perovskite Solar Cells Using Guanidinium and Octylammonium Spacer Cations. Sol. RRL *6*, 2200355. https://doi.org/10.1002/solr.202200355.
5. Xiong, S., Tian, F., Wang, F., Cao, A., Chen, Z., Jiang, S., Li, D., Xu, B., Wu, H., Zhang, Y., et al. (2024). Reducing Nonradiative Recombination for Highly Efficient Inverted Perovskite Solar Cells via a Synergistic Bimolecular Interface. Nat. Commun. *15*, 5607. https://doi.org/10.1038/s41467-024-50019-3.
6. Chen, R., Wang, J., Liu, Z., Ren, F., Liu, S., Zhou, J., Wang, H., Meng, X., Zhang, Z., Guan, X., et al. (2023). Reduction of Bulk and Surface Defects in Inverted Methylammonium- and Bromide-Free Formamidinium Perovskite Solar Cells. Nat. Energy *8*, 839–849. https://doi.org/10.1038/s41560-023-01288-7.
7. Jiang, Q., Zhao, Y., Zhang, X., Yang, X., Chen, Y., Chu, Z., Ye, Q., Li, X., Yin, Z., and You, J. (2019). Surface Passivation of Perovskite Film for Efficient Solar Cells. Nat. Photonics *13*, 460–466. https://doi.org/10.1038/s41566-019-0398-2.
8. Sidhik, S., Wang, Y., De Siena, M., Asadpour, R., Torma, A.J., Terlier, T., Ho, K., Li, W., Puthirath, A.B., Shuai, X., et al. (2022). Deterministic Fabrication of 3D/2D Perovskite Bilayer Stacks for Durable and Efficient Solar Cells. Science *377*, 1425–1430. https://doi.org/10.1126/science.abq7652.
9. Giza, M., Kozikov, A., Lalaguna, P.L., Hutchinson, J.D., Verma, V., Vella, B., Kumar, R., Hill, N., Sirbu, D., Arca, E., et al. (2024). Illuminating the Devolution of Perovskite Passivation Layers. Small Struct. *5*, 2400234. https://doi.org/10.1002/sstr.202400234.
10. Tang, J., Tian, W., Zhao, C., Sun, Q., Zhang, C., Cheng, H., Shi, Y., and Jin, S. (2022). Imaging the Moisture-Induced Degradation Process of 2D Organolead Halide Perovskites. ACS Omega *7*, 10365–10371. https://doi.org/10.1021/acsomega.1c06989.

11. Fang, H., Yang, J., Tao, S., Adjokatse, S., Kamminga, M.E., Ye, J., Blake, G.R., Even, J., and Loi, M.A. (2018). Unravelling Light-Induced Degradation of Layered Perovskite Crystals and Design of Efficient Encapsulation for Improved Photostability. Adv. Funct. Mater. *28*, 1800305. https://doi.org/10.1002/adfm.201800305.
12. Petrulevicius, J., Yang, Y., Liu, C., Steponaitis, M., Kamarauskas, E., Daskeviciene, M., Bati, A.S.R., Malinauskas, T., Jankauskas, V., Rakstys, K., et al. (2024). Asymmetric Triphenylethylene-Based Hole Transporting Materials for Highly Efficient Perovskite Solar Cells. ACS Appl. Mater. Interfaces *16*, 7310–7316. https://doi.org/10.1021/acsami.3c17811.
13. Du, S., Huang, H., Lan, Z., Cui, P., Li, L., Wang, M., Qu, S., Yan, L., Sun, C., Yang, Y., et al. (2024). Inhibiting Perovskite Decomposition by a Creeper-Inspired Strategy Enables Efficient and Stable Perovskite Solar Cells. Nat. Commun. *15*, 5223. https://doi.org/10.1038/s41467-024-49617-y.
14. Zhou, Q., Liang, L., Hu, J., Cao, B., Yang, L., Wu, T., Li, X., Zhang, B., and Gao, P. (2019). High-Performance Perovskite Solar Cells with Enhanced Environmental Stability Based on a (p-FC 6 H 4 C 2 H 4 NH 3) 2 [PbI 4] Capping Layer. Adv. Energy Mater. *9*, 1802595. https://doi.org/10.1002/aenm.201802595.
15. Chen, H., Teale, S., Chen, B., Hou, Y., Grater, L., Zhu, T., Bertens, K., Park, S.M., Atapattu, H.R., Gao, Y., et al. (2022). Quantum-Size-Tuned Heterostructures Enable Efficient and Stable Inverted Perovskite Solar Cells. Nat. Photonics *16*, 352–358. https://doi.org/10.1038/s41566-022-00985-1.
16. Zhou, H., Cai, K., Yu, S., Wang, Z., Xiong, Z., Chu, Z., Chu, X., Jiang, Q., and You, J. (2024). Efficient and Stable Perovskite Mini-Module via High-Quality Homogeneous Perovskite Crystallization and Improved Interconnect. Nat. Commun. *15*, 6679. https://doi.org/10.1038/s41467-024-50962-1.
17. Zhao, K., Liu, Q., Yao, L., Değer, C., Shen, J., Zhang, X., Shi, P., Tian, Y., Luo, Y., Xu, J., et al. (2024). Peri-Fused Polyaromatic Molecular Contacts for Perovskite Solar Cells. Nature *632*, 301–306. https://doi.org/10.1038/s41586-024-07712-6.
18. Schlipf, J., Hu, Y., Pratap, S., Bießmann, L., Hohn, N., Porcar, L., Bein, T., Docampo, P., and Müller-Buschbaum, P. (2019). Shedding Light on the Moisture Stability of 3D/2D Hybrid Perovskite Heterojunction Thin Films. ACS Appl. Energy Mater. *2*, 1011–1018. https://doi.org/10.1021/acsaem.9b00005.
19. Wu, G., Liang, R., Ge, M., Sun, G., Zhang, Y., and Xing, G. (2022). Surface Passivation Using 2D Perovskites toward Efficient and Stable Perovskite Solar Cells. Adv. Mater. *34*, 2105635. https://doi.org/10.1002/adma.202105635.
20. Sirbu, D., Balogun, F.H., Milot, R.L., and Docampo, P. (2021). Layered Perovskites in Solar Cells: Structure, Optoelectronic Properties, and Device Design. Adv. Energy Mater. *11*, 2003877. https://doi.org/10.1002/aenm.202003877.
21. Chen, P., Bai, Y., Wang, S., Lyu, M., Yun, J.H., and Wang, L. (2018). In Situ Growth of 2D Perovskite Capping Layer for Stable and Efficient Perovskite Solar Cells. Adv. Funct. Mater. *28*, 1706923. https://doi.org/10.1002/adfm.201706923.
22. Tanuma, S., Powell, C.J., and Penn, D.R. (1994). Electron Inelastic Mean Free Paths in Compounds. J. Surf. Anal. *21*, 165–176. https://doi.org/10.1384/jsa.26.106.
23. Powell, C.J., and Jablonski, A. (2010). NIST Electron Inelastic-Mean-Free-Path Database - Version 1.2 (National Institute of Standards and Technology).
24. Arca, E., Kehoe, A.B., Veal, T.D., Shmeliov, A., Scanlon, D.O., Downing, C., Daly, D., Mullarkey, D., Shvets, I.V., Nicolosi, V., and Watson, G.W. (2017). Valence Band Modification of Cr2O3 by Ni-Doping: Creating a High Figure of Merit p-Type TCO. J. Mater. Chem. C *5*, 12610–12618. https://doi.org/10.1039/c7tc03545d.
25. Forster-Tonigold, K., Buchner, F., Bansmann, J., Behm, R.J., and Groß, A. (2022). A Combined XPS and Computational Study of the Chemical Reduction of BMP-TFSI by Lithium. Batter. Supercaps *5*, e202200307. https://doi.org/10.1002/batt.202200307.
26. Zhang, Z., Qiao, L., Meng, K., Long, R., Chen, G., and Gao, P. (2023). Rationalization of Passivation Strategies toward High-Performance Perovskite Solar Cells. Chem. Soc. Rev. *52*, 163–195. https://doi.org/10.1039/d2cs00217e.
27. Teale, S., Degani, M., Chen, B., Sargent, E.H., and Grancini, G. (2024). Molecular Cation and Low-Dimensional Perovskite Surface Passivation in Perovskite Solar Cells. Nat. Energy *9*, 779–792. https://doi.org/10.1038/s41560-024-01529-3.
28. Cacovich, S., Vidon, G., Degani, M., Legrand, M., Gouda, L., Puel, J.B., Vaynzof, Y., Guillemoles, J.F., Ory, D., and Grancini, G. (2022). Imaging and Quantifying Non-Radiative Losses at 23% Efficient Inverted Perovskite Solar Cells Interfaces. Nat. Commun. *13*, 2868. https://doi.org/10.1038/s41467-022-30426-0.
29. Oner, S.M., Sezen, E., Yordanli, M.S., Karakoc, E., Deger, C., and Yavuz, I. (2022). Surface Defect Formation and Passivation in Formamidinium Lead Triiodide (FAPbI3) Perovskite Solar Cell Absorbers. J. Phys. Chem. Lett. *13*, 324–330. https://doi.org/10.1021/acs.jpclett.1c03645.
30. Tan, S., Yavuz, I., Weber, M.H., Huang, T., Chen, C.H., Wang, R., Wang, H. C., Ko, J.H., Nuryyeva, S., Xue, J., et al. (2020). Shallow Iodine Defects Accelerate the Degradation of α-Phase Formamidinium Perovskite. Joule *4*, 2426–2442. https://doi.org/10.1016/j.joule.2020.08.016.
31. Lanzetta, L., Aristidou, N., and Haque, S.A. (2020). Stability of Lead and Tin Halide Perovskites: The Link between Defects and Degradation. J. Phys. Chem. Lett. *11*, 574–585. https://doi.org/10.1021/acs.jpclett.9b02191.
32. Wang, J., Liu, L., Chen, S., Qi, L., Zhao, M., Zhao, C., Tang, J., Cai, X., Lu, F., and Jiu, T. (2022). Growth of 1D Nanorod Perovskite for Surface Passivation in FAPbI3 Perovskite Solar Cells. Small *18*, 2104100. https://doi.org/10.1002/smll.202104100.
33. Proppe, A.H., Wei, M., Chen, B., Quintero-Bermudez, R., Kelley, S.O., and Sargent, E.H. (2019). Photochemically Cross-Linked Quantum Well Ligands for 2D/3D Perovskite Photovoltaics with Improved Photovoltage and Stability. J. Am. Chem. Soc. *141*, 14180–14189. https://doi.org/10.1021/jacs.9b05083.
34. Schmid, M., Steinrück, H., and Gottfried, J.M. (2014). A New Asymmetric Pseudo-Voigt Function for More Efficient Fitting of XPS Lines. Surf. Interface Anal. *46*, 505–511. https://doi.org/10.1002/sia.5521.
35. Major, G.H., Fairley, N., Sherwood, P.M.A., Linford, M.R., Terry, J., Fernandez, V., and Artyushkova, K. (2020). Practical Guide for Curve Fitting in X-Ray Photoelectron Spectroscopy. J. Vac. Sci. Technol. A *38*, 061203. https://doi.org/10.1116/6.0000377.